Fluid-supported elastic sheet under compression: Multifold solutions

Leonardo Gordillo[1,*] and Edgar Knobloch[2,†]
[1]*Departamento de Física, Universidad de Santiago de Chile, Av. Ecuador 3493, Estación Central, Santiago, Chile*
[2]*Department of Physics, University of California at Berkeley, Berkeley, California 94720, USA*

(Received 25 February 2018; published 17 April 2019)

The properties of a hinged floating elastic sheet of finite length under compression are considered. Numerical continuation is used to compute spatially localized buckled states with many spatially localized folds. Both symmetric and antisymmetric states are computed and the corresponding bifurcation diagrams determined. Weakly nonlinear analysis is used to analyze the transition from periodic wrinkles to singlefold and multifold states and to compute their energy. States with the same number of folds have energies that barely differ from each other and the energy gap decreases exponentially as localization increases. The stability of the different competing states is studied and the multifold solutions are all found to be unstable. However, the decay time into solutions with fewer folds can be so slow that multifolds may appear to be stable.

DOI: 10.1103/PhysRevE.99.043001

I. INTRODUCTION

Recent experiments [1] have shown that an elastic sheet on the surface of a liquid undergoes a series of transitions when compressed in the longitudinal direction: For small compression the sheet deforms into a periodic array of wrinkles; with increasing compression the deformation of the sheet becomes more and more nonlinear and the deformation spontaneously localizes. This process continues until the sheet makes contact with itself.

These experiments have stimulated several efforts at modeling this sequence of transitions [2–5]. The equilibrium configurations are described by a fourth-order equation for the deformation angle as a function of arclength. This equation, as well as others describing post-buckling phenomena of elastic media under compression [6] and torsion [7,8], is of Swift-Hohenberg type and its solutions bear a number of similarities to existing analysis of steady states of the Swift-Hohenberg equation with a quadratic nonlinearity [9], or equivalently to the small amplitude behavior of the quadratic-cubic Swift-Hohenberg equation (SH23) as described, for instance, in Refs. [10,11]. Specifically, on an infinite domain one expects that the primary instability to the wrinkled state is accompanied by the simultaneous appearance of *two* branches of spatially localized solutions, one characterized by deformation that peaks in the center of the domain and the other that dips in the center. The theory tells us that on an infinite domain these states are described by the normal form for the reversible Hopf bifurcation (in space) with 1:1 spatial resonance [12]. In particular, the branches of localized solutions are initially exponentially close to one another [13–15], but gradually separate as the compression of the sheet increases and the solutions begin to localize.

Of course, in the experiments the sheet is of finite length. In this case existing theory shows that the 1:1 reversible Hopf bifurcation breaks apart into a primary bifurcation to a wrinkled state followed, at small amplitude, by a secondary bifurcation that creates a pair of spatially modulated wrinkled states, one with maxima in the center and the other with minima in the center. This bifurcation is an example of an Eckhaus instability of the periodic wrinkled state and its dependence on the domain length has been studied in detail [16]. In particular, it is known that subsequent secondary bifurcations lead to so-called multipulse states, i.e., states with more than one localized structure within the available domain [17]. However, since the periodically wrinkled state does not exhibit a saddle-node bifurcation the correspondence with SH23 does not extend to larger amplitude states; in particular, homoclinic snaking [10,11] is absent.

In this paper we use the similarity between the present problem and the Swift-Hohenberg equation to identify new classes of localized wrinkled structures on finite domains [18]. We focus on the case of a thin elastic sheet allowing us to neglect its contribution to the gravitational potential energy when its is deformed. In this case the model equation is odd in the dependent variable, a symmetry respected by the hinged boundary conditions we employ. As a consequence the system admits four types of localized states instead of the two mentioned above: two even parity states under spatial reflection and two odd parity states. Of these the even states correspond to deformation that either peaks or dips in the center of the domain while the odd parity states consist of symmetry-related peak-trough combinations. Consequently the system exhibits *four* branches of spatially localized states, and so its properties in fact resemble more closely those of the small amplitude states in the cubic-quintic Swift-Hohenberg equation [19,20] rather than those of the quadratic-cubic Swift-Hohenberg equation.

Each of these solutions is a singlefold solution, with a fold either in the center of the sheet or split between the two end points. However, the problem also admits a vast array of

*leonardo.gordillo@usach.cl
†knobloch@berkeley.edu

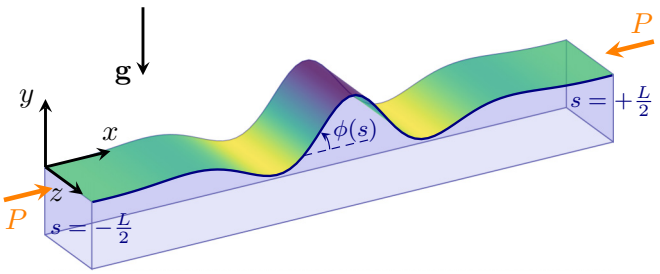

FIG. 1. Schematic view of the formation of a wrinkled pattern on an elastic sheet over a fluid substrate under compression. The shape of the sheet can be parametrized in terms of the local angle $\phi(s)$ that the sheet forms with the horizontal. The parameter s represents the arclength along the sheet, whose total length L is fixed.

multifold states consisting of both identical and nonidentical folds at different locations along the sheet. We compute here both singlefold and multifold states using numerical continuation techniques that have proved invaluable in studies of the Swift-Hohenberg equation, as well as weakly nonlinear theory of the type first employed in the present context in [5], and discuss the stability properties of these distinct states.

The paper is organized as follows. In Sec. II we summarize the basic properties of the model we use and introduce periodic solutions for both infinite sheets and for finite sheets with hinged boundary conditions. In Sec. III, we study in detail the wrinkle-to-fold transition, using both numerical continuation and weakly nonlinear analysis. The word *fold* is here employed to mean a strongly spatially localized deformation. We compute fold solutions with both zero and nonzero deformation at the center of the domain, as well as multifold structures, and incorporate the results into bifurcation diagrams of both periodic (wrinkles) and localized (fold) solutions. In Sec. IV, we analyze the properties of these structures in greater detail, and obtain expressions for the energy gap between singlefold symmetric and singlefold antisymmetric solutions in terms of the compression and the sheet length. We also provide a complete stability analysis of both singlefold and multifold states based on energy principles and show that localized folds interact through weak attraction or repulsion resulting in slow evolution of multifold states towards a singlefold state. Our conclusions are summarized in Sec. V.

Our results extend the work of Refs. [2,21] to finite domains and the analysis of Refs. [5,22] to multifold states.

II. GOVERNING EQUATIONS AND PERIODIC SOLUTIONS

A. Floating elastica under compression

A detailed derivation of floating-elastica equations from the fundamental principles of elasticity and hydrostatics can be found in Refs. [2,5]. Consider an infinitely thin elastic sheet of length L and bending modulus B on the surface of a semi-infinite incompressible liquid of density ρ. In static equilibrium under gravity, a compression Δ in the x direction will deform the sheet in the y direction as shown in Fig. 1, thereby elevating some of the liquid. The shape of the sheet can be parametrized in terms of the arclength s and the local angle $\phi(s)$ between the sheet and the horizontal axis. Cartesian coordinates $[x(s), y(s)]$ are related to this parametrization through $x(s) = \int_{-\frac{L}{2}}^{s} \cos\phi(s)\,ds$, $y(s) = \int_{-\frac{L}{2}}^{s} \sin\phi(s)\,ds$. Accordingly, the total energy stored (per unit of length in the z direction) due to the deformation is

$$E[\phi] = \int_{-L/2}^{+L/2} ds \left(\frac{1}{2}B\dot{\phi}^2 + \frac{1}{2}\rho g y^2 \cos\phi\right), \tag{1}$$

where the dot denotes derivative with respect to s and g is the acceleration due to gravity. The assumptions of this model are standard for post-buckling analysis [1,5]: the elastic sheet is very thin, and can therefore be considered to be incompressible [23,24]. Consequently, deformations under compression only occur in the normal direction to the sheet. These are resisted by a bending stiffness as described by the first term in the total strain energy (1), the bending energy in the sheet. The second represents the gravitational potential energy of the fluid raised by the deformation of the sheet. Thus, in this approach it is the fluid weight that provides the restoring force, in contrast to a potential energy proportional to y^2 alone that is appropriate for delamination of a sheet on an elastic substrate. The influence of a substrate on the wrinkling and folding process is addressed by Brau *et al.* [25]. Since the compression is assumed to be quasistatic, dynamical aspects of the system such as the kinetic energy or shear dissipation are absent from the formulation. In particular, the viscosity of the liquid plays no role in the problem. The sheet shape is in turn linked to the total compression Δ through

$$\Delta[\phi] = \int_{-L/2}^{+L/2} ds\,(1 - \cos\phi). \tag{2}$$

Thus, the load P required to keep the system in equilibrium is equal to $dE/d\Delta$.

The natural lengthscale of the system, $\lambda = [B/(\rho g)]^{1/4}$, can be used to nondimensionalize the quantities x, y, s, Δ, and L. It follows that the wavelength of the wrinkles that emerge after compression is of order λ, a law that is followed over more than four orders of magnitude (see Supporting Online Material in Ref. [1]). Likewise, the energy per unit length E can be scaled by B/λ and P by B/λ^2, leading to a simpler version of Eq. (1) with $B = \rho g = 1$. These scales determine the order of magnitude of E and P when the sheet is compressed. Specifically, in the macroscopic experiments by Pocivavsek *et al.* [1] with polyester and latex sheets $B \approx 10^{-4}\,\mathrm{N\,m}$, $\rho \approx 10^3\,\mathrm{kg/m^3}$, and $\lambda \approx 10^{-2}\,\mathrm{m}$ implying that the energy and load per unit length are, respectively, $E \approx 10^{-2}\,\mathrm{J/m}$ and $P \approx 1\,\mathrm{N/m}$. Thus, the load P dominates capillary forces (the liquid-air surface tension is $\sigma \approx 0.07\,\mathrm{N/m}$) which are therefore neglected.

We study quasistatic deformations of an elastic sheet under the following two conditions: (i) a fixed load P (*dead loading*), or (ii) fixed compression Δ (*rigid loading*). An equation for the shape of the sheet, $\phi(s)$, can be derived in both cases using a Lagrangian approach as shown in Refs. [2,3]. Whether minimizing the functional $E[\phi]$, the energy, for given Δ (rigid loading) or, equivalently, minimizing the functional $G[\phi] \equiv E - P\Delta$, the free energy, for given P (dead loading), one finds that $\phi(s)$ satisfies

$$\ddddot{\phi} + \tfrac{3}{2}\dot{\phi}^2\ddot{\phi} + p\ddot{\phi} + \sin\phi = 0, \tag{3}$$

where p depends on the boundary conditions. We adopt here hinged boundary conditions, i.e., the conditions $y|_{\pm L/2} = \ddot{y}|_{\pm L/2} = 0$ (or, equivalently, $\dot{\phi}|_{\pm L/2} = \dddot{\phi}|_{\pm L/2} = 0$), so p is related to the static load P by [5]

$$P = p\cos\phi(\pm L/2) - \ddot{\phi}(\pm L/2)\sin\phi(\pm L/2). \tag{4}$$

With these boundary conditions the system is invariant under the transformations $\phi \to -\phi$ and $s \to -s$, which are linked to invariance with respect to $x \to -x$ and $y \to -y$.

Equation (3) conserves the following quantity along the sheet:

$$H[\phi] = \dddot{\phi}\dot{\phi} - \tfrac{1}{2}\ddot{\phi}^2 + \tfrac{3}{8}\dot{\phi}^4 + \tfrac{1}{2}p\dot{\phi}^2 - \cos\phi.$$

For hinged sheets $H = -\frac{1}{2}\ddot{\phi}^2|_{\pm L/2} - \cos\phi|_{\pm L/2}$. Throughout this article both dead and rigid loading approaches will be considered and the results will therefore be represented either in terms of the quantities (P, G) or (Δ, E), as appropriate. The difference between these two approaches is of fundamental importance in the stability analysis discussed in Sec. IV.

B. Exact solutions for an infinite sheet

Despite the presence of nonlinear terms, Eq. (3) admits explicit exact solutions for the case of an infinite sheet. Two families of spatially *localized* solutions can be found [2]: a family of symmetric solutions,

$$\phi_s(s) = 4\arctan\left[\frac{\kappa\sin k(s-s_0)}{k\cosh\kappa(s-s_0)}\right], \tag{5}$$

and a family of antisymmetric solutions,

$$\phi_a(s) = 4\arctan\left[\frac{\kappa\cos k(s-s_0)}{k\cosh\kappa(s-s_0)}\right]. \tag{6}$$

Here $s = s_0$ corresponds to the symmetry point while $k = \frac{1}{2}\sqrt{2+P}$ and $\kappa = \frac{1}{2}\sqrt{2-P}$, i.e., the solutions exist only for $P < 2$. Evaluation in the limit $s \to \pm\infty$ shows that for this case $P = p$. The extra parameter s_0 is a result of the invariance of the infinite sheet under transformations of the form $s \to s + \text{const}$. In the literature, localized solutions are referred to as *folds*. Solutions (5) and (6) are members of a wider family of solutions, obtained by adding an extra phase to the trigonometric function, i.e.,

$$\phi_f(s) = 4\arctan\left[\frac{\kappa\cos[k(s-s_0)-\varphi_f]}{k\cosh\kappa(s-s_0)}\right]. \tag{7}$$

Thus, the symmetric and antisymmetric solutions correspond to the particular cases $\varphi_f = \pi/2$ and $\varphi_f = 0$, respectively. The asymmetric family $(\varphi_f \neq 0, \pi/2)$ has been shown to describe the shape of an elastic sheet when extracted from a fluid bath [21].

Moreover, explicit exact periodic solutions on an infinite sheet can be found in terms of Jacobi elliptic functions,

$$\phi(s) = 2\arcsin[k\,\mathrm{sn}_k(qs - \vartheta_0)], \tag{8}$$

or, equivalently,

$$y(s) = \frac{2k}{q}\,\mathrm{cn}_k(qs - \vartheta_0), \tag{9}$$

and these exist for $0 < k < 1$. The quantity q is related to k and the static load P by the implicit relation

$$P = q^2 + (1-2k^2)q^{-2}. \tag{10}$$

Thus, $q^2 - q^{-2} < P < q^2 + q^{-2}$. The solution in Eq. (8) has a period equal to $4K(k)/q$, where $K(k)$ is the complete elliptic integral of the first kind. Periodic solutions are usually referred to as *wrinkles* in the literature, cf. [25,26] and references therein.

C. Explicit periodic solutions for finite sheets

Exact periodic solutions of Eq. (3) for finite sheets can easily be found by matching properly both ϑ_0 and the period of solution (8) with the boundary conditions. For hinged boundary conditions, it follows that

$$\vartheta_0 = \nu_n K(k), \quad q_n = \frac{2nK(k)}{L}, \quad n = 1, 2, 3..., \tag{11}$$

where $\nu_n = 1$ for n odd and $\nu_n = 0$ for n even (see Ref. [5] for details). As expected, the finiteness of the sheet discretizes the parameter q into discrete families $q_n(k)$ labeled by the index n (the number of half-periods of the solution). Solutions of this type will be referred to as ϕ_n. The parameter k quantifies the amplitude of the solution as measured, for example, by the compression per unit length, $\overline{\Delta} \equiv \Delta/L$:

$$\overline{\Delta} = 2I(k). \tag{12}$$

Here $I(k) \equiv 1 - E(k)/K(k)$ and $E(k)$ is the complete elliptic integral of the second kind. Remarkably, this expression does not depend on n.

The energy per unit length, $\overline{E} \equiv E/L$, of the family of periodic solutions is given by

$$\overline{E} = 2\left(q_n^2 + q_n^{-2}\right)[k^2 - I(k)] - [a_k - b_k I(k)], \tag{13}$$

where $a_k = 8q_n^{-2}(k^4 + k^2)/15$ and $b_k = 16q_n^{-2}(k^4 - k^2 + 1)/15$. The free energy $\overline{G} = \overline{E} - P\overline{\Delta}$ now follows from Eqs. (12) and (13). For a given n and L, Eqs. (10)–(13) determine $(\overline{\Delta}, \overline{E}, \overline{G}, P)$ in terms of the single continuous parameter k. Figure 2 depicts the resulting solution branches in the $(\overline{\Delta}, \overline{E})$ plane for $L = 20\pi$ and different n values.

Periodic solutions for finite sheets bifurcate from the trivial state $\phi(s) = 0$ at $k = 0$. Since $E(0) = K(0) = \pi/2$, each periodic branch ϕ_n bifurcates from the P axis at

$$P_n^* = q_n^2 + q_n^{-2} \tag{14}$$

and $\Delta_n^* = 0$. Thus, $P_n^* \geqslant 2$ with equality at $n = L/\pi$. To determine which solution emerges spontaneously when the sheet is compressed, we expand Eqs. (12) and (13) around $k = 0$, yielding $\overline{\Delta}(k) \approx k^2$ and $\overline{E} \approx (q_n^2 + q_n^{-2})k^2$, respectively. It follows that $\overline{E} \approx (q_n^2 + q_n^{-2})\overline{\Delta}$. The branch with minimal energy in the $(\overline{\Delta}, \overline{E})$ plane near the trivial state is that which minimizes the slope $q_n^2 + q_n^{-2} \approx P_n^*$ of the energy. Hence, the branch bifurcating at the lowest P_n^* value is the only one that is stable in the vicinity of the primary bifurcation.

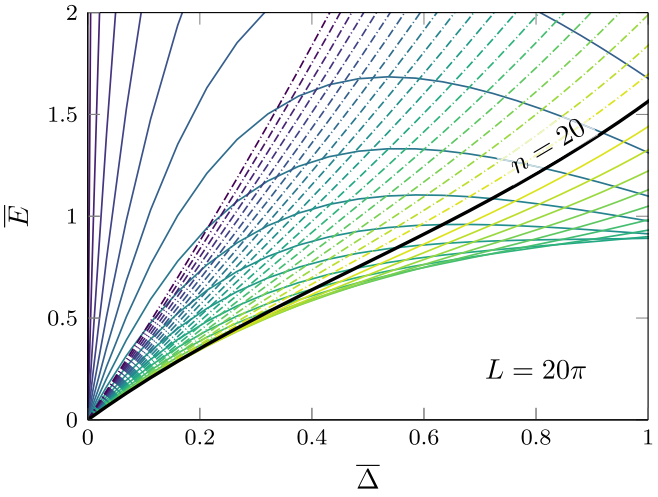

FIG. 2. Branches of periodic states ϕ_n in the $(\overline{\Delta}, \overline{E})$ plane for a sheet of fixed length $L = 20\pi$. Each curve corresponds to a different family $q_n(k)$, $n = 1, 2, ..., 40$, with k related to $\overline{\Delta}$ by Eq. (12). The branch for $n = 20$ has the least energy near the common bifurcation point at the origin. Dash-dotted branches correspond to $n > 20$.

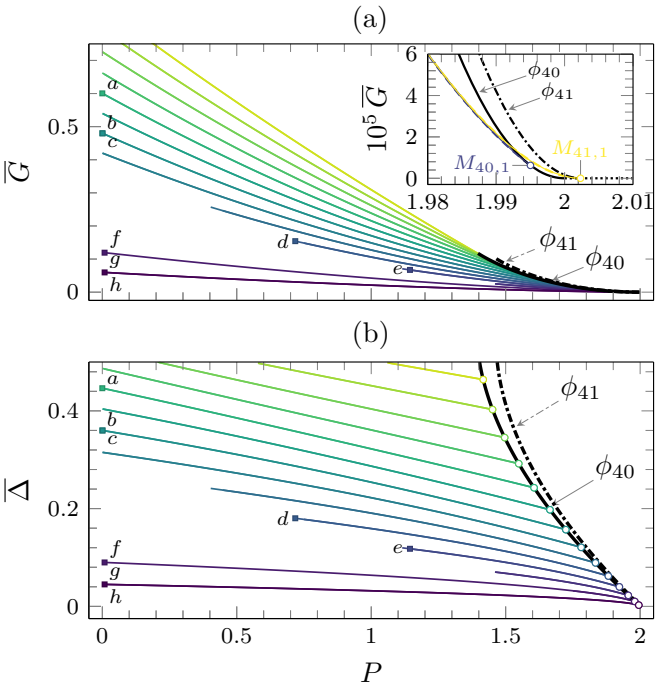

FIG. 3. Results from numerical continuation of Eq. (3) subject to hinged boundary conditions, showing different solution branches in the form (a) $\overline{G}(P)$ and (b) $\overline{\Delta}(P)$, both for $L = 40\pi$. The thick black line represents the periodic state $n = 40$, which undergoes several bifurcations as P decreases (see text for details). The other branches represent multifold states. The solutions shown in Fig. 4 correspond to the labeled symbols ■ (b-c and g-h overlap). The inset in (a) shows the region near the origin where the symmetric and antisymmetric fold solutions first appear. Bifurcation points are marked as ○. The $n = 41$ periodic branch (dashed line) is also displayed. No discernible difference between the results of the analysis of Sec. III B (thin lines) and the numerical continuation results is seen.

The branches ϕ_n and ϕ_{n+1} bifurcate simultaneously from the trivial state whenever $L_{(n,n+1)} = \pi\sqrt{n(n+1)}$ and do so at $P^*_{(n,n+1)} = 2 + [n(n+1)]^{-1}$. These conditions define the range of L for which the nth solution is stable: $L_{(n-1,n)} < L < L_{(n,n+1)}$. As $L \to \infty$, the width of this range converges to π and its center to πn.

Far from the primary bifurcation, corresponding to $k = 0$, other branches may display lower energies than the branch that minimizes P^*_n. This is illustrated in Fig. 2, which shows that the lower n branches eventually cross the $n = 20$ branch as $\overline{\Delta}$ increases.

III. FOLDS IN FINITE SHEETS

A. Numerical continuation of localized patterns

Since no explicit exact localized solutions of Eq. (3) exist for elastic sheets of finite length and hinged boundary conditions, we employ numerical continuation [27,28] to follow different solution types of this problem through parameter space. For this purpose, we implemented Eq. (3) in the code AUTO [29] with hinged boundary conditions, with the independent variable s transformed so the original half domain $[-L/2, 0]$ becomes $[0, 1]$. Since the quantities $(\overline{\Delta}, \overline{E}, \overline{G}, P)$ are all functions of the parameters (p, L) of the system, we plot the results as a function of P instead of p, for fixed length $L = l\pi$ $(l \in \mathbb{R})$.

Numerical continuation requires an initial guess. Taking advantage of the existence of explicit periodic solutions, we performed continuation on a 128-point spatial grid starting from solution (8) for a given n and a high value of k, i.e., ϕ_n far from the trivial state. The code was tuned to detect bifurcation points along this branch as P increases toward the onset value P^*. Figures 3(a) and 3(b) display the branches ϕ_{40} and ϕ_{41} in black, both for $L = 40\pi$. Each periodic branch displays a set of bifurcation points with decreasing separation as P increases towards P^*. For ϕ_{40} these bifurcation points are shown in Fig. 3(b). These bifurcation points will be referred to as $M_{n,m}$, where the integer n specifies the primary periodic state and the integer m counts the bifurcations from this state starting from the primary bifurcation P^*_n. Thus, $M_{40,1}$ denotes the secondary bifurcation closest to P^*_{40}.

At each of the secondary bifurcation points $M_{n,m}$ we switched the branch direction and ran the numerical continuation for decreasing P until $P = 0$ was attained. The new branches are also displayed in Fig. 3 but now in color. Some of the solutions far from the bifurcation points $M_{n,m}$ are depicted in Fig. 4. A simple inspection [see inset in Fig. 3(a)] shows that the branch starting at $M_{40,1}$ corresponds to a localized antisymmetric fold while that starting at $M_{41,1}$ is a symmetric fold. The former bifurcation point is located quite far from P^*_{40}, i.e., at finite amplitude, while the latter lies very close to P^*_{41}. At this value the ϕ_{41} state barely departs from the trivial state. For $L = 41\pi$ the situation is the opposite: the symmetric fold is the one that bifurcates at finite amplitude (from the ϕ_{41} branch), while the antisymmetric fold bifurcates at a very small amplitude (from the ϕ_{42} branch). Despite this difference the resulting branches approach one another rapidly as P decreases (Δ increases) becoming essentially indistinguishable as $P \to 0$ [Fig. 3(a), inset].

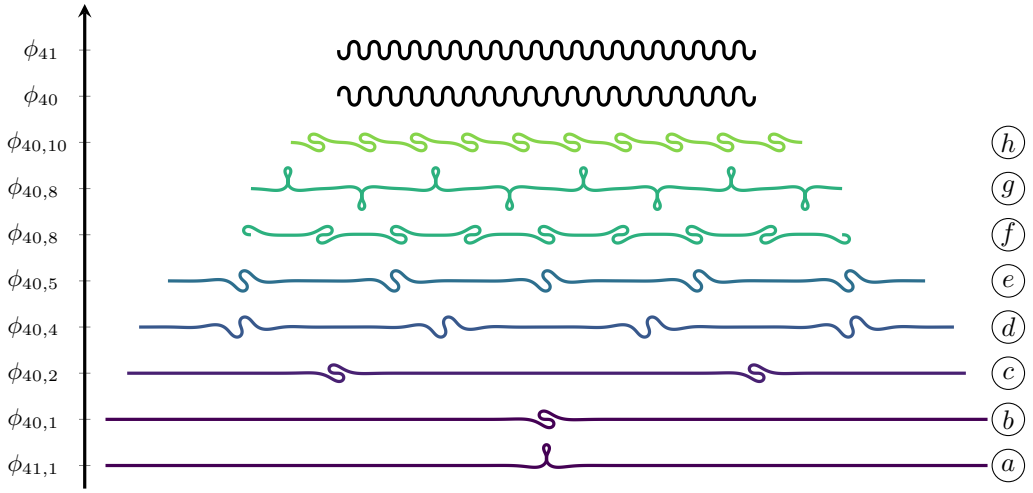

FIG. 4. Antisymmetric solutions (b–h) from numerical continuation for different values of m defined in the text and $n = 40$ computed on a domain of length $L = 40\pi$. The location of each solution in parameter space is indicated in Fig. 3. The solutions acquire additional folds as m increases. The symmetric solution $\phi_{41,1}$ (a) bifurcates from the $n = 41$ periodic state, and does so very close to the trivial state, as shown in the inset in Fig. 3(a). The periodic solutions ϕ_{40} and ϕ_{41} at high compression ($\overline{\Delta} = 0.55$) are included for reference.

Solutions $\phi_{n,m}$ with $m > 1$ represent m-fold solutions, i.e., arrays of m equispaced folds. Examples are shown in Fig. 4. Although reported in Ref. [22], these multifold solutions have not been described in detail. Multifold solutions $\phi_{n,m}$ for a fixed l do not exist for arbitrary n and m. For instance, for $l = 40$, singlefold solutions ($m = 1$) are observed only for $n = 40$ and 41 while twofold solutions ($m = 2$) are only found for $n = 39, 40, 41, 42$. In general, $2m + 2$ solutions with m folds were detected for n varying from $l - m + 1$ to $l + m$.

B. Weakly modulated solutions

Multiscale analysis describes successfully several features of this system and, in particular, the wrinkle-to-fold transition [3,30]. Herein, we use this approach to understand the emergence of the solutions obtained in Sec. III A. The system is assumed to be subject to hinged boundary conditions and finite. The domain of s is mapped into $s \in [0, L]$ for the sake of simplicity in the application of the boundary conditions.

We seek multiscale solutions of Eq. (3) in the form

$$y(s) = \sum_{j=1}^{\infty} \epsilon^j u_j(s, S = \epsilon s), \tag{15}$$

where the functions u_j are of $\mathcal{O}(1)$ and ϵ is a small parameter measuring the distance from some primary instability threshold, $\epsilon^2 \equiv p^* - p$. Since $\phi(s) = \arcsin(\partial_s y)$ with ∂_s now replaced by $\partial_s + \epsilon\partial_S$, Eq. (3) generates a hierarchy of equations for the functions $u_j(s, S)$. The first three equations are

$$\begin{aligned}
\mathcal{O}(\epsilon^1): &\quad \mathcal{L}_{p^*}\partial_s u_1 = 0,\\
\mathcal{O}(\epsilon^2): &\quad \mathcal{L}_{p^*}\partial_s u_2 = -\mathcal{L}'_{p^*}\partial_s u_1,\\
\mathcal{O}(\epsilon^3): &\quad \mathcal{L}_{p^*}\partial_s u_3 = -\mathcal{L}'_{p^*}\partial_s u_2 - \mathcal{N}_{p^*}\partial_s u_1,
\end{aligned} \tag{16}$$

where the fourth-order linear operators $\mathcal{L}_{p^*}$ and $\mathcal{L}'_{p^*}$ and the nonlinear operator $\mathcal{N}_{p^*}$ are, respectively, defined as

$$\begin{aligned}
\mathcal{L}_{p^*} w &\equiv \left(\partial_s^4 + p^*\partial_s^2 + 1\right)w,\\
\mathcal{L}'_{p^*} w &\equiv \left(5\partial_s^4 + 3p^*\partial_s^2 + 1\right)w,\\
\mathcal{N}_{p^*} w &\equiv \tfrac{1}{2}\dddot{w}w^2 + 10\ddot{w}w'' + \tfrac{15}{2}\dot{w}w'' + 3\ddot{w}^2 w\\
&\quad + 4\ddot{w}\dot{w}w - \ddot{w} + p^*\left[\tfrac{1}{2}\ddot{w}w^2 + 3w'' + \dot{w}w\right].
\end{aligned}$$

Here the overdots denote derivatives with respect to s, while the primes denote derivatives with respect to S. At the instability threshold $p^* = 2$ the linear operators reduce to $\mathcal{L}_2 \equiv (\partial_s^2 + 1)^2$ and $\mathcal{L}'_2 \equiv (\partial_s^2 + 1)(5\partial_s^2 + 1)$ and have a common kernel spanned by the null eigenfunctions of the second-order linear operator $\partial_s^2 + 1$. In this case the $\mathcal{O}(\epsilon^1)$ solution of Eq. (16) is $u_1(s, S) = A(S)\sin(s - \theta)$, i.e., the dominant term $u_1(s, S)$ is a carrier wave with wave number $q = 1$ modulated by a slowly varying envelope $A(\epsilon s)$. It now follows that the right side of the $\mathcal{O}(\epsilon^2)$ equation vanishes, and hence that $u_2 \equiv 0$. An equation for $A(S)$ is therefore obtained by imposing a solvability condition at $\mathcal{O}(\epsilon^3)$. A straightforward calculation yields

$$A'' - \tfrac{1}{4}A + \tfrac{1}{8}A^3 = 0. \tag{17}$$

Equation (17) has two solutions given by Jacobi elliptic functions,

$$\epsilon A_{\mathrm{dn}}(S) = 4\epsilon\kappa_{\mathrm{dn}}\,\mathrm{dn}_k(\kappa_{\mathrm{dn}}S - \vartheta_{\mathrm{dn}}), \tag{18}$$

$$\epsilon A_{\mathrm{cn}}(S) = 4\epsilon\kappa_{\mathrm{cn}}\tfrac{1}{2}k\,\mathrm{cn}_k(\kappa_{\mathrm{cn}}S - \vartheta_{\mathrm{cn}}), \tag{19}$$

where ϑ is an arbitrary phase and

$$\epsilon^2\kappa_{\mathrm{dn}}^2 = \tfrac{1}{4}(2 - p)(2 - k^2)^{-1}, \tag{20}$$

$$\epsilon^2\kappa_{\mathrm{cn}}^2 = \tfrac{1}{4}(2 - p)(2k^2 - 1)^{-1}. \tag{21}$$

TABLE I. Set of combinations of θ, ϑ, L, and $\epsilon\kappa$ that fulfill hinged boundary conditions. Both l and m are positive integers. The functions $y_{\mathrm{dn}}(s)$ and $y_{\mathrm{cn}}(s)$ are given by the product of $\sin(s-\theta)$ and ϵA_{dn} and ϵA_{cn}, respectively. Solutions that do not display folds at the boundaries are indicated by the symbol † (in the y_{dn} case, the required m value in the last column must be even).

	θ	ϑ	L	$\epsilon\kappa L$
$y_{\mathrm{dn}}(s)$	$0^{\dagger}, \pi$	$0, K(k)^{\dagger}$	$l\pi$	$mK(k)^{\dagger}$
$y_{\mathrm{cn}}(s)$	$0, \pi$	$\pm K(k)$	$l\pi$	$2mK(k)$
			$(l+\frac{1}{2})\pi$	$2(m+\frac{1}{2})K(k)$
	$\pm\frac{1}{2}\pi^{\dagger}$	$0, K(k)^{\dagger}$	$l\pi$	$2mK(k)$
			$(l+\frac{1}{2})\pi$	$2(m+\frac{1}{2})K(k)$

Thus, each solution branch is parametrized by k, just as for the periodic case in Sec. II C. The final step is to multiply the expressions for the modulation amplitude A by the carrier wave, $\sin(qs-\theta)$, and match the result to the hinged boundary conditions. Note that both the modulation amplitude and the carrier wave are periodic functions of s.

1. Wave number and phase selection

Since the wave number $q=1$, the weakly modulated solutions satisfy hinged boundary conditions only for a simple set of combinations of θ, ϑ, L, and $\epsilon\kappa$, displayed in Table I. This set can be identified on realizing that the chosen boundary conditions are satisfied if and only if one of the two periodic functions, either the trigonometric or the elliptic one, has a node (zero) at the boundary while the other has an antinode (local maximum or minimum) at the same location.

Since both elliptic functions localize as $k \to 1$, some of the solutions from Table I may display folds at the boundaries. This happens whenever the trigonometric function has a node at the boundary. These types of solutions were also detected in our numerical continuation. However, in the remainder of this article, and for the sake of simplicity, we restrict our analysis to solutions that do not display folds at the boundaries. These remaining solutions are indicated in Table I by a † symbol.

2. Branches in parameter space

The weakly modulated solutions $y(s) = A(\epsilon s)\sin(s-\theta)$ can be used to build expansions for the static load P, the energy per unit length $\overline{E}$, the compression per unit length $\overline{\Delta}$ and the free energy per unit length $\overline{G}$ for a sheet of finite length L. For a static load P the condition $p = 2-\epsilon^2$ translates into $P = 2-\epsilon^2+\mathcal{O}(\epsilon^4)$ using Eq. (4) and the solutions obtained in Sec. III B 1. Accordingly, $(\overline{E}, \overline{\Delta}, \overline{G}) = \sum_{j=1}\epsilon^j(\overline{E}_j, \overline{\Delta}_j, \overline{G}_j)$. The expressions for $(\overline{E}_j, \overline{\Delta}_j, \overline{G}_j)$ can be simplified by averaging over one period of the fast oscillation, e.g., $\int_0^L ds\, \sin^2(s)A(\epsilon s) \approx \frac{1}{2}\int_0^L ds\, A(\epsilon s)$. As a consequence, the first and third order terms all vanish and the remaining quantities only depend on the envelope $A(S)$. The following expressions for the quantities $P, \overline{G}, \overline{\Delta}, \overline{E}$ to $\mathcal{O}(\epsilon^4)$ are obtained:

$$
\begin{aligned}
P &= 2-\epsilon^2+\mathcal{O}(\epsilon^4),\\
\overline{G} &= \tfrac{1}{2}\epsilon^4\big[\tfrac{1}{2}\overline{A^2}+2\overline{A'^2}-\tfrac{1}{8}\overline{A^4}\big],\\
\overline{\Delta} &= \tfrac{1}{4}\epsilon^2\overline{A^2}+\tfrac{1}{4}\epsilon^4\big[\tfrac{3}{16}\overline{A^4}+\overline{A'^2}\big],\\
\overline{E} &= \tfrac{1}{2}\epsilon^2\overline{A^2}+\tfrac{1}{2}\epsilon^4\big[3\overline{A'^2}+\tfrac{1}{16}\overline{A^4}\big].
\end{aligned}
\tag{22}
$$

Here the overbar indicates a spatial average over the slow variable S. After replacing A by A_{dn} or A_{cn} from Eqs. (18) and (19), all the averaged quantities can be expressed in terms of the complete elliptic integrals $K(k)$ and $I(k)$ (see Appendix A). For our reduced set of solutions, $\epsilon = 2mK(k)/(\kappa L)$, where κ is either κ_{dn} or κ_{cn}. Hence, all solution branches are fully parametrized in terms of k. Inversion of Eqs. (20) and (21) yields an expression for the static load. For $q=1$ we obtain, through $\mathcal{O}(\epsilon^4)$,

$$
\begin{aligned}
\begin{bmatrix}P_{\mathrm{dn}}\\ P_{\mathrm{cn}}\end{bmatrix} &= 2-\frac{2^4m^2}{L^2}K^2(k)\begin{bmatrix}2-k^2\\ 2k^2-1\end{bmatrix},\\
\begin{bmatrix}\overline{G}_{\mathrm{dn}}\\ \overline{G}_{\mathrm{cn}}\end{bmatrix} &= \frac{2^8m^4}{3L^4}K^4(k)\begin{bmatrix}3-k^2-2(2-k^2)I(k)\\ 3k^4-k^2-2(2k^2-1)I(k)\end{bmatrix},\\
\begin{bmatrix}\overline{\Delta}_{\mathrm{dn}}\\ \overline{\Delta}_{\mathrm{cn}}\end{bmatrix} &= \frac{2^4m^2}{L^2}K^2(k)\begin{bmatrix}1-I(k)\\ k^2-I(k)\end{bmatrix}\\
&\quad+\frac{2^6m^4}{3L^4}K^4(k)\begin{bmatrix}9-2k^2-7(2-k^2)I(k)\\ 9k^4-2k^2-7(2k^2-1)I(k)\end{bmatrix},\\
\begin{bmatrix}\overline{E}_{\mathrm{dn}}\\ \overline{E}_{\mathrm{cn}}\end{bmatrix} &= \frac{2^5m^2}{L^2}K^2(k)\begin{bmatrix}1-I(k)\\ k^2-I(k)\end{bmatrix}\\
&\quad+\frac{2^7m^4}{3L^4}K^4(k)\begin{bmatrix}3+2k^2-5(2-k^2)I(k)\\ 3k^4+2k^2-5(2k^2-1)I(k)\end{bmatrix}.
\end{aligned}
$$

We use the above expressions to characterize the dnoidal and cnoidal solutions in a bifurcation diagram, and the parameter k as a measure of their amplitude. In particular, the condition $k \to 0$ determines the threshold for the appearance of each solution type.

C. Wrinkle-to-fold transition

Experiments have shown that an elastic sheet over a fluid substrate undergoes a wrinkle-to-fold transition when continuously compressed from its original length [1]. The wrinkle-to-fold transition is characterized by the emergence of a localized fold from a periodic pattern. Figure 5 shows the critical loads P_n^* for the appearance of a periodic state with $n = 38, 39, \ldots, 42$ wavelengths in the domain (solid lines), as well as the secondary bifurcation thresholds $M^{\mathrm{dn}}_{n=l,m=1}$ for the appearance of the lowest energy dnoidal states ($m=1$) obtained from the $k \to 0$ limit of the dnoidal solutions of the previous section (orange filled circles). In contrast, the cnoidal solutions bifurcate from the periodic states within an $\mathcal{O}(L^{-3})$ neighborhood of $L = L_{(n-1,n+1)}$, the crossing points for like-parity modes $n-1$ and $n+1$. The predicted bifurcation thresholds $M^{\mathrm{cn}}_{n=l,m=1}$ (purple open circles) are also obtained from the $k \to 0$ limit of the corresponding analytical solution. These bifurcation points and the analytical expressions for the small amplitude solutions present nearby were used as an input into a numerical continuation routine and used to extend these thresholds to noninteger values of L/π ($M_{n,m=1}$ in Fig. 5). Numerical continuation reveals that the

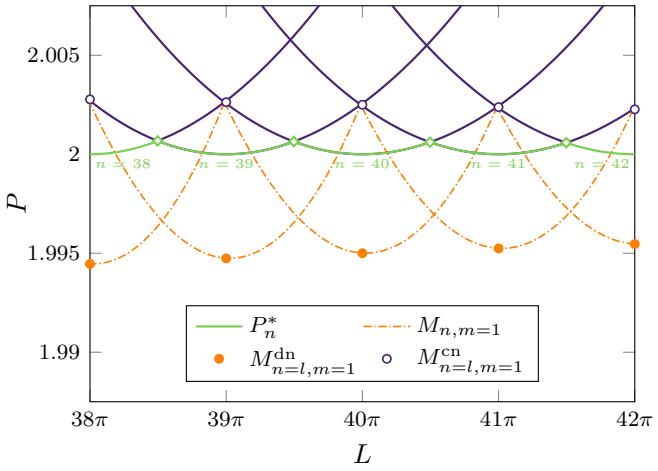

FIG. 5. Bifurcation thresholds in the (L, P) plane: primary bifurcation thresholds P_n^* to periodic states ϕ_n together with secondary bifurcation thresholds $M_{n,m=1}$ to dnoidal states (dash-dotted lines) obtained by numerical continuation, each for $n = 38, 39, ..., 42$. The symbol $\diamond$ denotes codimension-two transitions between n and $n+1$ periodic wrinkle states. The orange filled (respectively, purple open) circles indicate the multiscale analysis predictions of bifurcations to dnoidal (respectively, cnoidal) states when $n = l$ (with $l = L/\pi \in \mathbb{Z}^+$).

$M_{n,m=1}$ curves resemble parabolas with vertices located in the vicinity of $M^{\rm dn}_{n=l,m=1}$. These parabolas extend between the codimension-two points $L_{(n-2,n)}$ and $L_{(n,n+2)}$ (or approximately, between $M^{\rm cn}_{n=l-1,m=1}$ and $M^{\rm cn}_{n=l+1,m=1}$). Also indicated are the codimension-two points $L = L_{(n,n+1)}$ (open green diamonds) corresponding to the crossing of periodic modes n and $n+1$, i.e., the points at which the primary bifurcation to a symmetric wrinkle state changes to an antisymmetric wrinkle state as L changes. The curves $M_{n,m=1}$ and P_n^*, as well as the predicted locations $M^{\rm dn}_{n=l,m=1}$ and $M^{\rm cn}_{n=l,m=1}$, are all compressed towards the $P = 2$ axis as L increases.

As shown in Fig. 5 the multiscale analysis generates a discrete set of bifurcation points instead of the continuous curves of bifurcation points obtained by numerical continuation. The solid curves for $L \in (l\pi, (l+1)\pi)$, $l \in \mathbb{Z}^+$, can only be obtained via numerical continuation. This limitation of the multiscale analysis has its origin in the structure of the equations analyzed in Sec. III B, which requires $l \in \mathbb{Z}^+$ to satisfy simultaneously the boundary conditions and the cancellation of the right-hand side of the $\mathcal{O}(\epsilon^2)$ equation in Eq. (16). If we instead follow Refs. [3,5] and minimize the functional $\overline{G}$ on the assumption that $y(s) = A(S)\cos(qs)$, we obtain Eq. (17) when $q = 1$ and a similar equation to Eq. (17) but with q-dependent coefficients whenever $q > 1$. The latter, however, yields inaccurate solutions, which are an artifact of improper assumption on the s-dependence of $y(s)$ when $q > 1$.

D. The $\pi/2$-shifted localized branch

The exact nonlinear solutions in Eqs. (5) and (6) show that the symmetric and antisymmetric folds on an infinite sheet are equivalent from the energy point of view. Such states are therefore energetically degenerate. However, this is no longer the case on a finite sheet and the question arises whether a sheet whose wrinkle-to-fold transition yields a symmetric (antisymmetric) fold may also display an antisymmetric (symmetric) fold. Results from Sec. III B 2 provide hints about the dynamical features of these two states. For $l \in \mathbb{Z}^+$ symmetric and antisymmetric singlefold states (i.e., $n = l, m = 1$) can be understood in terms of the carrier wave phase θ. The idea is simple: since the Jacobi elliptic functions in Table I approximating the two solution types both peak at the center of the sheet, the choice of whether $\theta = 0$ or $\theta = \pi/2$ determines the symmetry of the central fold. For $n = l$ even (odd), the dnoidal (cnoidal) branch yields the antisymmetric (symmetric) singlefold state and the cnoidal (dnoidal) branch the symmetric (antisymmetric) state. However, there is an important difference between these two branches. The cnoidal branch, whose carrier wave is shifted by $\pi/2$ relative to the dnoidal branch, emerges from the trivial state through a primary bifurcation to the right of the primary bifurcation to the periodic state (and half as close to it as the dnoidal branch bifurcation on the left). The resulting predictions of the theory of Sec. III B 2 are displayed in the inset of Fig. 3(a) and compared there with the corresponding results from numerical continuation. The accuracy of the approach is very good.

The theoretical predictions show that in the limit $L \to \infty$ both branches merge into a single one in terms of (Δ, E, G, P). As L increases, the secondary bifurcation to dnoidal states is pushed downward along the primary periodic branch while the cnoidal bifurcation point is also pushed towards the primary bifurcation point. These two bifurcation points coalesce in the limit $L \to \infty$. The corresponding large amplitude dnoidal and cnoidal branches become rapidly very close as P decreases, a prediction that is confirmed by numerical continuation to values of ϵ far beyond $\epsilon = 1$, i.e., $P \ll 1$.

E. Multifold solutions

The modulation analysis carried out above also provides a clearer picture of the emergence of multifold ($m \geqslant 2$) solutions for $l \equiv (L/\pi) \in \mathbb{Z}^+$. The condition $q = 1$ requires that $n = l$, where the labels n and m, introduced in Sec. III A, represent the carrier and envelope wave numbers, respectively. The bifurcations for $m \geqslant 2$ follow the same principle as the branches of localized states when $m = 1$, i.e., the dnoidal m-branch bifurcates from a periodic state ϕ_n at finite amplitude while the corresponding cnoidal m-branch bifurcates from the periodic state ϕ_{n+m} at a very small amplitude, and to the right of the primary bifurcation to ϕ_n and half as close to it as the bifurcation to the dnoidal branch. For example, when $m = 2$ the cnoidal branch in general bifurcates from ϕ_{42} and does so very close to the point P^*_{42}, although it may bifurcate directly from the trivial state but only at the crossing point of P^*_{38} and P^*_{42}. Likewise, the bifurcation points to the $m \geqslant 2$ dnoidal branches spread out from the primary bifurcation point to the nth periodic branch as m^2. We also used numerical continuation to follow the $M_{n,m}$ bifurcation points as a function of L as done in Sec. III C for $M_{n,1}$. Just as the singlefold cnoidal bifurcation point lies in the vicinity of $L_{(n-1,n+1)}$, the crossing point of the primary bifurcations to the $n-1$ and $n+1$ periodic branches, the m-fold cnoidal bifurcation point is located in the vicinity of $L_{(n-m,n+m)}$, the crossing

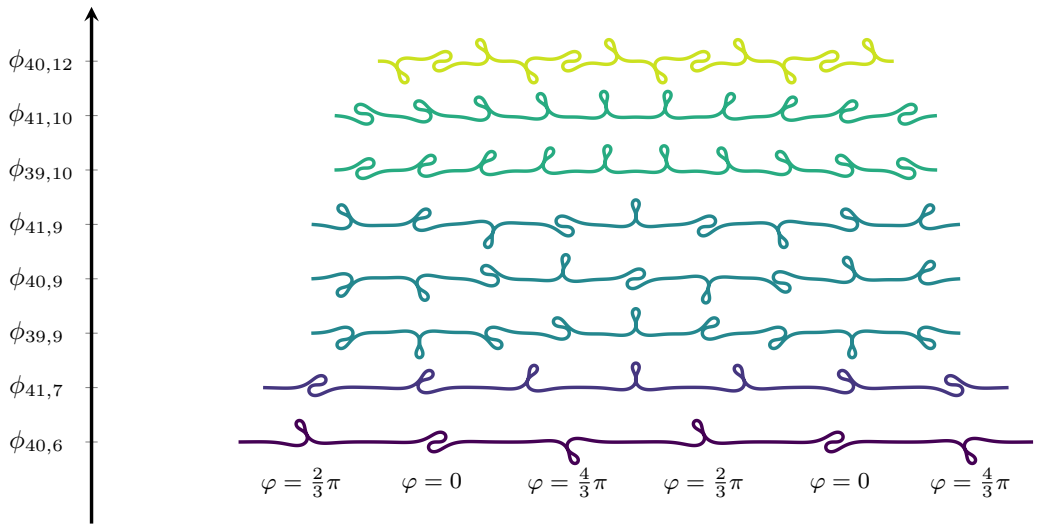

FIG. 6. A set of spatially modulated periodic solutions from numerical continuation for a sheet of length $L = 40\pi$ and different values of n and m. In all cases $P = 1$. The solutions are composed of distorted folds. While m determines the number of folds, n fixes the shape of each fold (see text for details). For the lowest state, the local phase of the carrier wave, φ_f, is indicated.

point of the primary bifurcations to the $n - m$ and $n + m$ periodic branches. Likewise, the $M_{n,m}$ bifurcation curves for noninteger L/π resemble parabolas with vertices near $M^{\rm dn}_{l=n,m}$ extending from $L_{(n-2m,n)}$ to $L_{(n,n+2m)}$. The range of existence of the parabola clarifies why the number of m-fold states observed is $2m + 2$ and which n values are allowed for a given m and L.

The analysis also reveals another interesting feature. The choice of l and m determines (a) if the solution consists of an array of symmetric or antisymmetric folds, and (b) the local shape of each fold. The rule for (a) is very simple: these states are allowed if l is divisible by m. For the dnoidal solutions, if l/m is even, the solutions will be an array of antisymmetric folds whereas for l/m odd the solution will be an array of symmetric folds with alternating orientation. If folds are allowed at both boundaries, then another possible solution, consisting of alternating antisymmetric folds for l/m even, can be observed. For $l = 40$, periodic multifold states are observed for $m = 2, 4, 5, 8, 10, 20$, as displayed in Fig. 4 ($m = 20$ is not shown). The figure also shows a state with folds at either boundary, for $m = 8$, to illustrate the complementary family of periodic solutions.

When l is not divisible by m the folds forming the array become distorted and resemble the family of arbitrary phase folds described in Ref. [21] for an infinite length sheet. The rule (b) for the local shape of each fold can be understood in terms of the phase φ_f in Eq. (7), which is now fixed by the carrier wave. The jth fold of the dnoidal solutions displays a local phase $\varphi_f = -l\pi(j - 1/2)/m$, whereas for the cnoidal solutions $\varphi_f = -\pi/2 - l\pi(j - 1/2)/m$. Accordingly, the fundamental period of an array of folds in a dnoidal solution is given by $2L/\mathrm{GCD}(l, 2m)$ while the fundamental period for cnoidal solutions is $L/\mathrm{GCD}(l, m)$ provided l is divisible by m and $L/\mathrm{GCD}(l, m)$ is odd, or $2L/\mathrm{GCD}(l, m)$ in all other cases. Examples of distorted folds are displayed in Fig. 6 for $L = 40\pi$. Solutions which do not satisfy $q = 1$, e.g., $\phi_{n=39,m}$ or $\phi_{n=41,m}$ in a $L = 40\pi$ domain, obey a similar rule for the local phase as that obtained by swapping the integer l for n, i.e., replacing l in φ_f by n to obtain $\phi_{n\neq l,m}$. Further analysis for this general case is required to understand this feature.

IV. DISCUSSION

A. Energy gap

The energy of the dnoidal and cnoidal branches for $l \in \mathbb{Z}^+$ and $n = l$ far from the bifurcation can be found by expanding the expressions for P, $\overline{G}$, $\overline{\Delta}$, and $\overline{E}$ obtained in Sec. III B 2 around $k = 1$. If we write $k = 1 - \xi$, $\xi \ll 1$, we then obtain

$$g_m \equiv \frac{1}{m}G^{\pm}_m(P) = \frac{8}{3}(2 - P)^{3/2}\left(1 \mp \frac{3}{2}\xi\right), \tag{23}$$

$$e_m \equiv \frac{1}{m}E^{\pm}_m(\Delta) = 2\delta_m - \frac{1}{48}\delta_m^3(1 \mp 3\xi), \tag{24}$$

where the $-$ $(+)$ corresponds to the dnoidal (cnoidal) branch and $\delta_m \equiv \Delta/m$ is the singlefold average compression. At leading order both branches have exactly the same energy. Equation (23) shows that, for fixed P (dead loading), the G spectrum is a set of equispaced free energies, where the quantity $g_m \approx \frac{8}{3}(2 - P)^{3/2}$ can be identified with the free energy of a single fold. However, for fixed compression Δ (rigid loading), the energy of a single fold is $e_m \approx 2\delta - \delta^3/48$. The energies display maxima at $\delta_{\max} = 2^{5/2}$, with $e_{\max} = 2^{9/2}/3$. Numerical continuation shows that this point is related to self-contact of the sheet. A comparison between the numerical results and the analytical approach at leading order is shown in Fig. 7 for $q = 1$. The overlap between the numerical continuation results and the analytical approximation is remarkable.

Figure 8 shows the difference between the $m = 1$ dnoidal and cnoidal branches obtained from numerical continuation and compares the result with the theoretical prediction obtained by inverting the series expansions for either P or Δ to

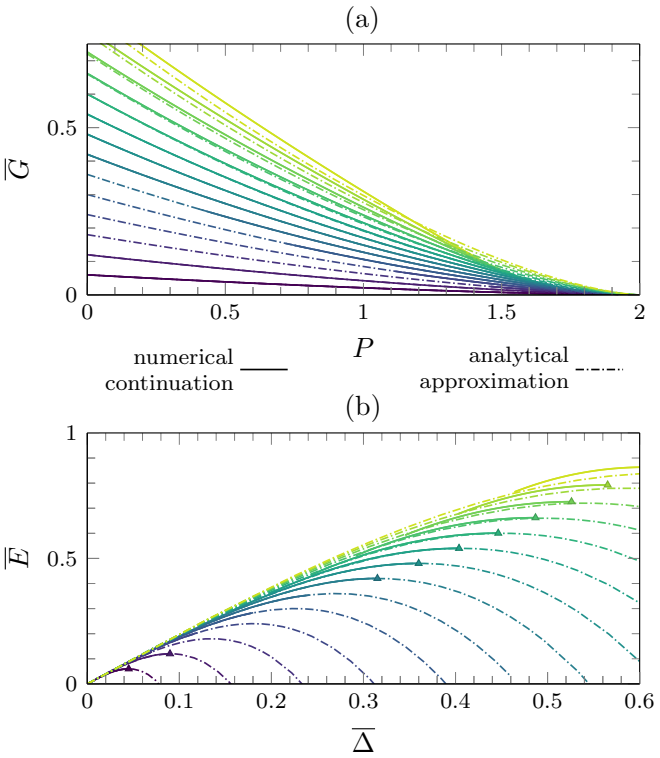

FIG. 7. Multifold branches for a sheet of length $L = 40\pi$ over a fluid substrate in (a) the $(P, \overline{G})$ plane and (b) the $(\overline{\Delta}, \overline{E})$ plane. Solid lines represent the numerical continuation results while the dash-dotted lines indicate the leading order analytical approximation. The numerical continuation was stopped at $P = 0$ [indicated by ▲ in (b)] in all cases, although the analytical approach extends beyond this point. The analytical approximation starts to depart from the numerical results only when the number of folds is very high, $m > 10$.

obtain ξ in terms P or Δ. The final result for the energy gap between the dnoidal and cnoidal branches is

$$\delta g_m \equiv g_m^+ - g_m^- = -64(2-P)^{\frac{3}{2}} \mathrm{e}^{-\frac{1}{2} l_m (2-P)^{\frac{1}{2}}}, \tag{25}$$

$$\delta e_m \equiv e_m^+ - e_m^- = -\delta_m^3 \mathrm{e}^{-\frac{1}{8} l_m \delta_m}, \tag{26}$$

where $l_m \equiv L/m$ can be identified as the spacing between the folds. The predicted exponential decay in both (P, G) and (Δ, E) planes matches the numerical results almost perfectly. The exponentially small residual difference is a consequence of the finite sheet size and can be thought of as arising from the interaction between the exponential tails of localized solutions [13]. Note that the functions in Eqs. (25) and (26) are nonmonotonic and with minima at $P \sim 2$ and $\delta_m \sim 0$ when L is large. These minima do not appear in the plots in Fig. 8 because these are restricted by the requirement that the necessary dnoidal and cnoidal solutions exist and the minima fall outside this parameter region. In fact, it can be shown, by combining Eqs. (25) and (26) with the expressions in Sec. III B 2, that within the existence region of the two solutions both δg_m and δe_m are monotonic for all m.

The general case $q \neq 1$ far from the bifurcation is more complicated and is not well described by the weak modulation approach. Numerical continuation shows that, at leading order, the energies for $q \neq 1$ are in fact exactly the same as those for the $q = 1$ branches: the solutions appear to shift their q toward $q = 1$ as $k \to 1$, a feature that is beyond the scope of the approach in Sec. III B.

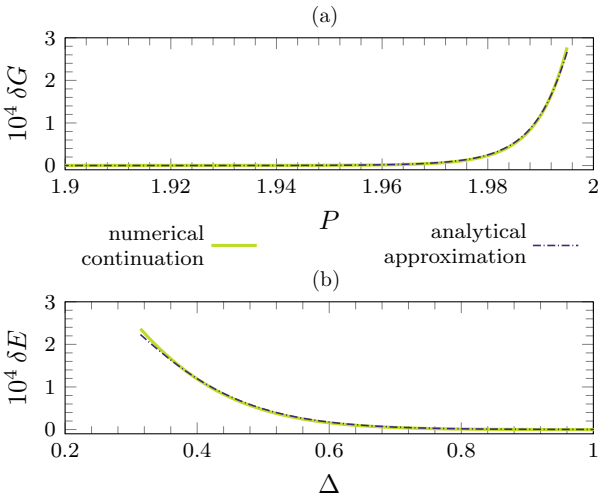

FIG. 8. Gap between the dnoidal and cnoidal singlefold solutions for $L = 40\pi$ in (a) the (P, G) plane and (b) the (Δ, E) plane. The analytical approximation (dash-dotted line) once again matches the numerical continuation results (solid line).

B. Stability analysis

The analysis carried out in the previous sections provides a framework for understanding how singlefold and multifold solutions bifurcate from periodic states. However, this type of analysis does not address the stability of the solutions, although we expect solutions with lowest energy such as the singlefold solution $\phi_{40,1}$ for $L = 40\pi$ to be stable. For example, it may happen that several solutions are stable simultaneously. Thus, a stability analysis provides a link between the theoretical predictions and observations in experiments.

To explore the stability properties of the solutions identified above, we carried out a numerical study based on a variational approach. Since the equations of a fluid-supported elastic sheet are static (time-independent), we consider a solution as stable if and only if it corresponds to a local minimum of energy in the space of functions satisfying all the constraints, as well as the boundary and symmetry conditions imposed by the problem formulation. The stability of a solution is thus guaranteed if the energy functional is positive definite in its vicinity, i.e., if and only if $E[\phi_0 + \delta\phi] > E[\phi_0]$, $\forall\, \delta\phi \in \mathbb{F}_\phi$, where E is defined as in Eq. (1), ϕ_0 is the solution under study, $\delta\phi \neq 0$ is the variation of ϕ_0 and $\mathbb{F}_\phi$ is the space of (continuous) functions such that $\phi_0 + \delta\phi$ satisfies the prescribed constraints (e.g., $\Delta[\delta\phi] = 0$ under rigid loading), and the boundary and symmetry conditions (hinged, symmetric, or antisymmetric).

For this purpose we introduce the inner product $(f, g) \equiv \int_{-L/2}^{L/2} f g ds$. It can then be shown (see Appendix B) that the

functionals E, G evaluated at $y = y_0 + \delta y$ can be written as

$$E[y] = E_0 + \left(\frac{\delta E}{\delta y}, \delta y\right) + \left(\delta y, \frac{\delta^2 E}{\delta y^2}\delta y\right) + \mathcal{O}(\delta y^3),$$

$$G[y] = G_0 + \left(\frac{\delta G}{\delta y}, \delta y\right) + \left(\delta y, \frac{\delta^2 G}{\delta y^2}\delta y\right) + \mathcal{O}(\delta y^3),$$

where $E_0 = E[\phi_0]$, $G_0 = G[\phi_0]$ and all the functional derivatives are evaluated at ϕ_0 (equivalently, $y = y_0$). The variation δy is related to the corresponding variation $\delta\phi$ by the geometrical relation $\partial_s(y + \delta y) = \sin(\phi + \delta\phi)$ (see Appendix B for further details). Similar relations can be written for P and Δ. By construction, the terms in E or G linear in δy vanish when $y = y_0$ is a solution of the original variational problem. Hence, under dead loading (P fixed) the solution is stable provided

$$\left(\delta y, \frac{\delta^2 G}{\delta y^2}\delta y\right) = \left(\delta y, \left[\frac{\delta^2 E}{\delta y^2} - P_0\frac{\delta^2 \Delta}{\delta y^2}\right]\delta y\right) > 0.$$

Here $P_0 = P[y_0]$. In the rigid loading case, P is no longer fixed and the stability condition becomes

$$\left(\delta y, \left[\frac{\delta^2 E}{\delta y^2} - P_0\frac{\delta^2 \Delta}{\delta y^2}\right]\delta y\right) - \delta P\left(\frac{\delta \Delta}{\delta y}, \delta y\right) > 0,$$

with an extra constraint imposed by the fixed compression:

$$\left(\frac{\delta \Delta}{\delta y}, \delta y\right) = 0.$$

Since the operator $\delta^2 G/\delta y^2$ in the square brackets is a real symmetric operator, the inner products behave as a quadratic form in function space. Thus, the spectral decomposition of the operator yields a set of (real) eigenvalues and the corresponding eigenfunctions containing information about the stability of the solution.

In practice, we first recovered ϕ_0 and the corresponding y_0 from the AUTO calculations and resampled them into an N vector. The derivative operators from Eqs. (B1)–(B3) were likewise discretized into $N \times N$ arrays using Fourier derivative matrices. Using these results, we built a discrete $N \times N$ matrix of the free energy functional $\delta^2 G/\delta y^2$, $\mathbf{G}_{N\times N}$. The stability of solutions in the dead loading case simply depends on the spectral decomposition of $\mathbf{G}_{N\times N}$, that is, on the eigenvalues of the standard eigenvalue problem

$$\mathbf{G}[\delta y] = \lambda[\delta y]. \tag{27}$$

The rigid loading case requires further work because of the extra constraint. In this case we discretized the compression condition by introducing a matrix $\Delta'_{N\times 1}$ as the discrete version of $\delta\Delta/\delta y$, and the $(N+1)\times(N+1)$ bordered Hessian matrix $\mathbf{H}$ given by

$$\mathbf{H} \equiv \begin{bmatrix} 0 & -\boldsymbol{\Delta}'_{1\times N} \\ -\boldsymbol{\Delta}'_{N\times 1} & \mathbf{G}_{N\times N} \end{bmatrix}.$$

As shown in Ref. [31], the stability problem can be studied via the generalized eigenvalue problem

$$\mathbf{H}\begin{bmatrix}\delta P \\ \delta y\end{bmatrix} = \lambda\begin{bmatrix} 0 & \mathbf{0}_{1\times N} \\ \mathbf{0}_{N\times 1} & \boldsymbol{I}_{N\times N}\end{bmatrix}\begin{bmatrix}\delta P \\ \delta y\end{bmatrix}. \tag{28}$$

Thus, the stability of a solution under dead or rigid loading can be tested by checking the signs of the eigenvalues of the standard [Eq. (27)] or generalized eigenvalue [Eq. (28)] problems, respectively. If all the eigenvalues are positive, then linear stability is guaranteed.

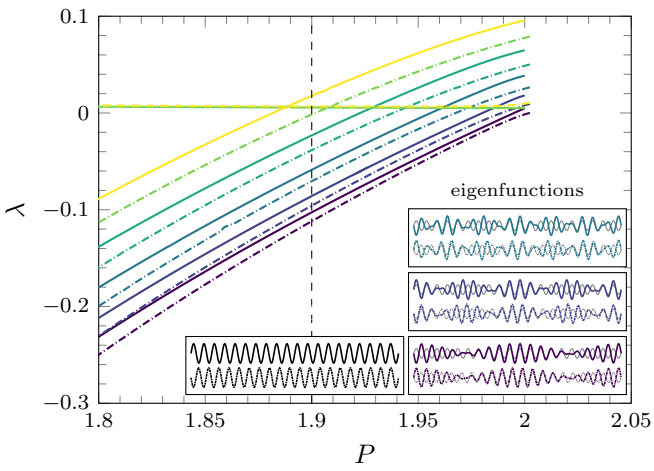

FIG. 9. Eigenvalues λ as a function of the load P for two periodic solutions: ϕ_{40} (solid lines) and ϕ_{41} (dash-dotted lines). The left inset shows the periodic solutions evaluated at $P = 1.9$ (vertical dashed line in main panel). The right insets show the eigenfunctions evaluated at the same value of P using the same color scheme as in the main panel. The insets show the ϕ_{40} eigenfunctions at the top (thick lines) and the ϕ_{41} eigenfunctions at the bottom (thin lines). The corresponding periodic solutions are plotted in black in the background for reference.

Within this framework, we now proceed to describe the stability properties of the solutions for a $L = 40\pi$ sheet. For dead loading, we confirmed that all the solutions obtained thus far from numerical continuation (wrinkle, singlefold and multifold) are unstable to amplitude modes, in agreement with the fact that $\partial G/\partial P < 0$ for all these branches. The rigid loading case is much more interesting, however. In the following section, we describe the stability properties of the periodic solutions ϕ_{40} and ϕ_{41}, the symmetric and asymmetric singlefold solutions $\phi_{40,1}$ and $\phi_{41,1}$, and the twofold solutions $\phi_{39,2}$, $\phi_{40,2}$, $\phi_{41,2}$ and $\phi_{42,2}$. For the sake of completeness, we also examined the stability of solutions displaying half-folds at the boundaries, which we denote by the superscript b. For instance, the solution $\phi^{(b)}_{40,1}$ has half-folds at $s = \pm L/2$, i.e., $\frac{1}{2} + \frac{1}{2} = 1$ complete fold.

1. Stability of periodic solutions

Figure 9 shows the six lowest eigenvalues λ as a function of the load P for the periodic solutions ϕ_{40} (solid lines) and ϕ_{41} (dashed lines). The corresponding eigenfunctions evaluated at $P = 1.9$ are shown in the right insets following the same color scheme as used for the eigenvalue curves. The figure indicates that the periodic solution ϕ_{40} becomes unstable at $P = 1.995$, when its lowest eigenvalue becomes negative. The corresponding eigenfunction represents a buckling mode that leads to either a centered singlefold state or a pair of half-folds on the boundaries. We will refer to these eigenfunctions as fold eigenmodes. At $P \approx 1.980$, a second eigenvalue becomes negative, which buckles the solution into a pair of folds (or a $\frac{1}{2} + 1 + \frac{1}{2}$-fold state); at $P \approx 1.956$, a third instability sets in,

buckling the solution into three folds or a $\frac{1}{2}+1+1+\frac{1}{2}$-fold state, etc. The points where these solutions cross $\lambda=0$ are consistent with the branch points identified using AUTO as leading to solutions that subsequently evolve into fold solutions. Similar behavior is observed for the periodic solution ϕ_{41}, with fold eigenvalues crossing $\lambda=0$ sequentially as the number of folds increases. Besides the fold eigenvalues all of which decrease monotonically as P decreases, a second family of eigenvalues is also present. However, these never cross $\lambda=0$ even though they decrease monotonically as P decreases. The associated eigenfunctions do not buckle the solution into localized folds but instead introduce spatial modulation on top of the periodic pattern. We conclude that the periodic solutions are stable with respect to spatial modulation, at least when the wavelength of the periodic state is close to the natural wavelength (no Eckhaus instability).

Figure 12(a) shows the construction of a $n=40$ pseudosolution arising from the second unstable fold mode. The pseudosolution is obtained by adding a multiple of the eigenfunction (here the multiple is ±1) to the periodic state ϕ_{40}. Panel (a) shows that when the multiple is $+1$ the instability suppresses the oscillations in the center and near the boundaries, leaving a $1+1$ state. When the multiple is -1 the result is a state resembling a $\frac{1}{2}+1+\frac{1}{2}$ state.

2. *Stability of singlefold solutions*

The corresponding diagram for singlefold solutions is shown in Fig. 10. The four singlefold solutions have positive eigenvalues and hence are all stable. The first two solutions $\phi_{40,1}$ and $\phi^{(b)}_{40,1}$, have identical eigenvalues, a consequence of the fact that $\phi^{(b)}_{40,1}$ can be obtained through a half-domain translation of $\phi_{40,1}$. This translation respects the boundary conditions at $s=\pm L/2$. The lowest eigenvalue of $\phi_{40,1}$ is inherited from the periodic branch ϕ_{40} and represents the amplitude mode of ϕ_{40} [Fig. 12(b)]. The second lowest eigenvalue is of particular interest, because its eigenmode is related to the splitting of the central fold into two [Fig. 12(c)]. These eigenmodes, which will be referred to as splitting eigenmodes, represent modulation of a carrier wave that shifts continuously with respect to the base state, with a π-phase shift at the center of the fold. With increasing amplitude this mode leads to growing separation of the central fold into two adjacent folds, in contrast to the usual fold eigenmodes corresponding to a 0 or π shift. The third eigenvalue is linked to a fold eigenmode which buckles the solution into a $\frac{1}{2}+1+\frac{1}{2}$ array. Larger eigenvalues show similar behavior involving larger numbers of folds. However, none of these modes is unstable, and so no finite amplitude solutions of this type are present.

The stability behavior the $\phi_{41,1}$ state is similar to that of $\phi_{40,1}$ although there are some important differences. First, the solution $\phi^{(b)}_{41,1}$ no longer corresponds to a simple half-domain shift of $\phi_{41,1}$: to satisfy symmetry conditions, a $\frac{\pi}{2}$ phase shift of the carrier wave plus an inversion of the solution in one half of the domain is also required. As a result the eigenvalues of $\phi_{41,1}$ and $\phi^{(b)}_{41,1}$ are no longer identical. The slight difference between them ($\lesssim 10^{-4}$) is due to the presence of a defect in the center of the domain in the latter case. The lowest eigenvalue mode is again related to the periodic solution, $\phi_{41,0}$. The next lowest eigenvalue mode is now a $1+1$ eigenmode while the third is a splitting eigenmode. Notice also that the second mode has the lowest eigenvalue for $P\lessapprox 1.982$ but this eigenvalue, like the others, remains positive and no instability is triggered.

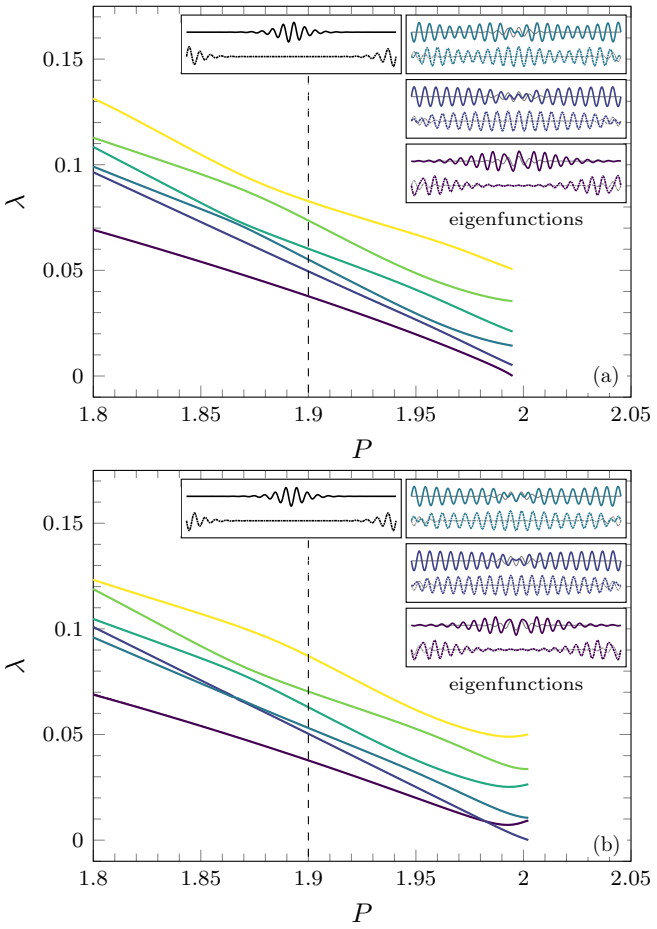

FIG. 10. Eigenvalues λ as a function of the load P for four singlefold solutions. (a) Symmetric fold: $\phi_{40,1}$ (solid lines) and $\phi^{(b)}_{40,1}$ (dash-dotted lines). (b) Antisymmetric fold: $\phi_{41,1}$ (solid lines) and $\phi^{(b)}_{41,1}$ (dash-dotted lines). As in Fig. 9, the left insets show the solutions evaluated at $P=1.9$ and those on the right show the eigenfunctions. The insets show centered fold eigenfunctions at the top (solid lines) and the boundary half-fold eigenfunctions at the bottom (dashed lines).

3. *Stability of twofold solutions*

We also studied the stability properties of the twofold solutions. The eigenvalues of the $\phi_{39,2}$, $\phi_{40,2}$, $\phi_{41,2}$, and $\phi_{42,2}$ solutions are shown in Fig. 11 (solutions with folds on the boundaries are also shown). All the twofold solutions are unstable displaying a single negative eigenvalue. At the bifurcation point to a twofold solution (e.g., at $P\approx 1.98$ for $\phi_{39,2}$) the amplitude eigenvalue inherited from the periodic state vanishes but becomes positive as P decreases just as in the singlefold case. However, this eigenvalue is passed by that of another mode in the vicinity of the bifurcation point (e.g., at $P\approx 1.975$ for $\phi_{39,2}$). The corresponding eigenmode is nonperiodic and remarkably interesting. For the $\phi_{41,2}$ and

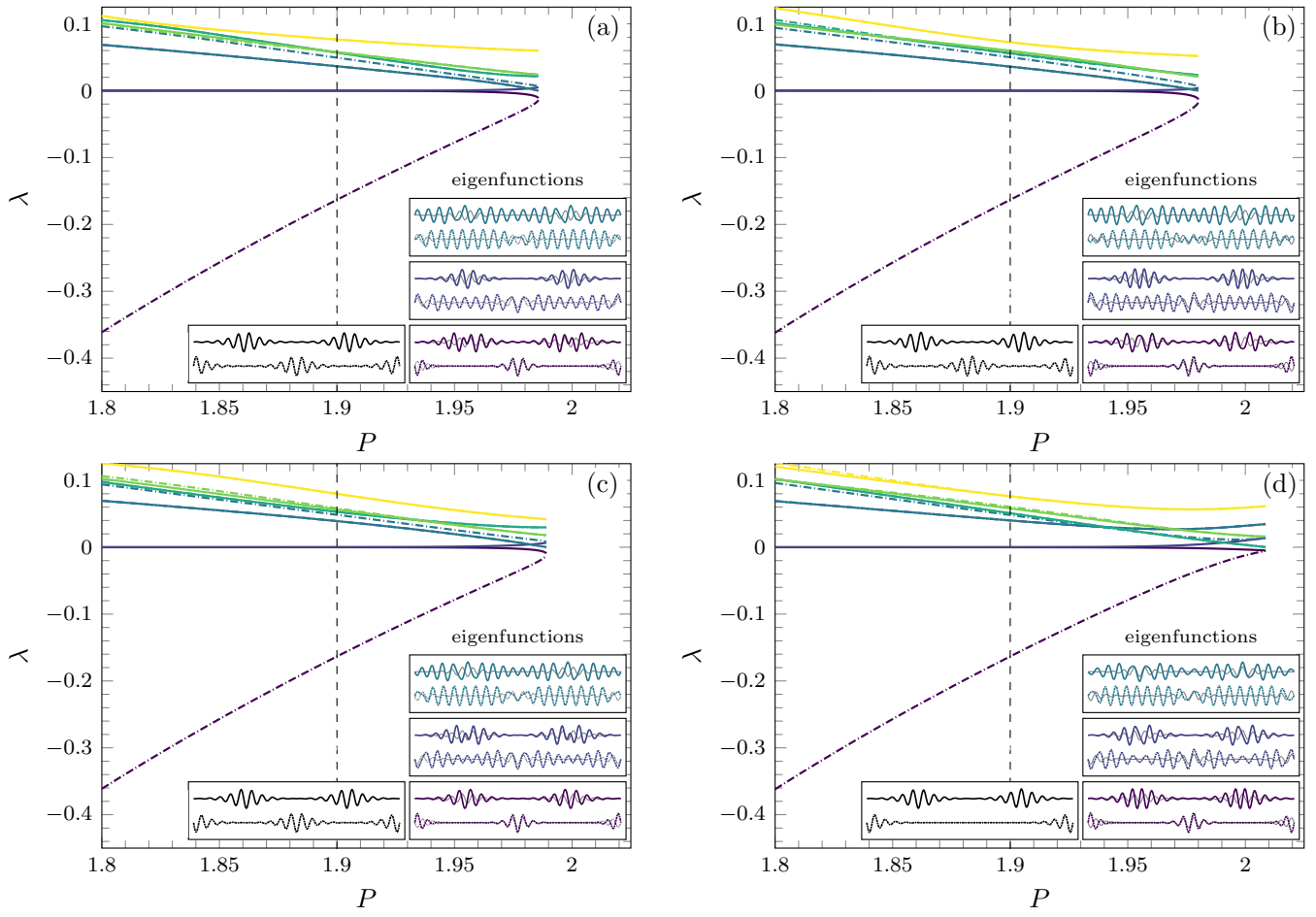

FIG. 11. Eigenvalues λ as a function of the load P for the eight twofold solutions. (*a*) $\phi_{39,2}$ (solid lines) and $\phi^{(b)}_{39,2}$ (dash-dotted lines). (*b*) $\phi_{40,2}$ (solid lines) and $\phi^{(b)}_{40,2}$ (dash-dotted lines). (*c*) $\phi_{41,2}$ (solid lines) and $\phi^{(b)}_{41,2}$ (dash-dotted lines). (*d*) $\phi_{42,2}$ (solid lines) and $\phi^{(b)}_{42,2}$ (dash dotted lines). As in Fig. 9, the left insets show the solutions evaluated at $P = 1.9$ and those on the right show the eigenfunctions. The insets show centered fold eigenfunctions at the top (solid lines) and the boundary half-fold eigenfunctions at the bottom (dashed lines).

$\phi_{42,2}$ solutions, these two lowest eigenvalue modes display the same modulation as the periodic solution but with a $\pm\frac{\pi}{2}$ shift in the carrier wave. Because of the localization of the folds, this feature is a reminiscent of a Goldstone translation mode. The eigenmode acts on the solutions by translating the left fold to the right ($+\frac{\pi}{2}$ shift) and the right fold to the left ($-\frac{\pi}{2}$ shift), or vice versa, without changing their shape. Consequently, we refer to this mode as a translational attraction (or repulsion) eigenmode. The other lowest eigenvalue mode is slightly different: on one side of each fold the mode displays a π shift while on the other side there is no phase shift. These eigenmodes also generate attraction (or repulsion) between folds but also change their shape. We refer to them as rolling attraction (or repulsion) eigenmodes. While in the translation mode both the carrier wave and the envelope translate, in the rolling case only the envelope shifts, resulting in a local deformation of the folds. The situation for $\phi_{39,2}$ and $\phi_{40,2}$ is similar with the difference that the translation and rolling eigenmodes change their order. Figures 12(d) and 12(e) show pseudosolutions that indicate the tendencies represented by these modes. We conclude that the twofold states are in all cases unstable and that the instability takes the form of a gradual approach of the twofolds, ultimately resulting in a stable singlefold state. The manifestation of the instability may be very slow, however, as it depends on the energy difference between these two states. This conclusion is supported by the fact that the unstable eigenvalue of the twofold state approaches zero from below, asymptotically exponentially, as P decreases. This comes as no surprise since the twofolds can only interact via the overlapping tails of their profiles and these are exponentially small when the folds are sufficiently far apart, a fact that suggests that as the solutions increasingly localize (i.e., P decreases), the time required for the system to reach the singlefold state becomes exponentially long. This decay may arise through attraction or repulsion via either the translation or rolling eigenmodes. In contrast, twofold solutions with folds on the boundary decay into a singlefold state much more rapidly as the folds at the boundary decay leaving only the fold at the center.

We emphasize, finally, that since our stability analysis is based on energy arguments it does not allow us to determine whether an isolated pair of folds will attract or repel. To answer this question, we would need to set up a time-dependent version of the problem and study the nonlinear evolution of the unstable modes (rolling and translational) that we have

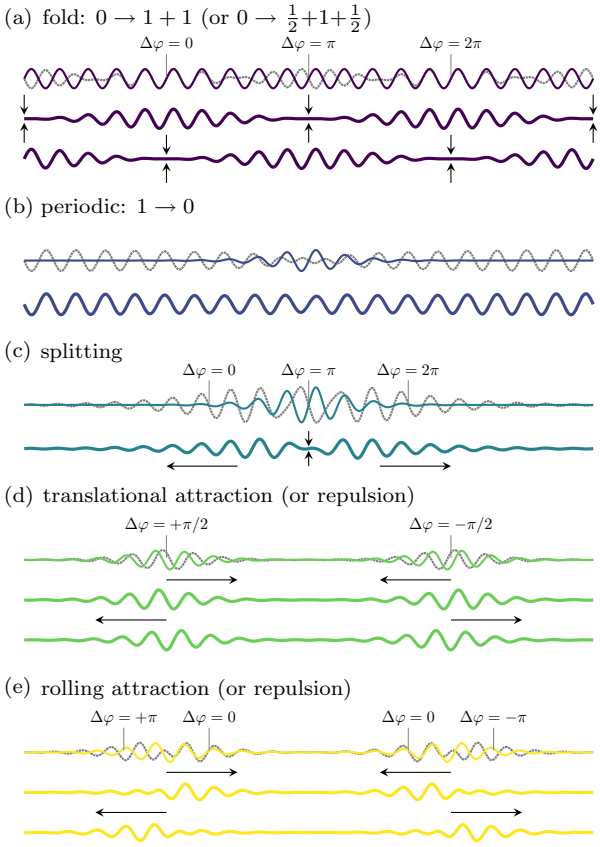

FIG. 12. Examples of base states (top solid lines) and the corresponding eigenmodes (top dash-dotted lines) and pseudosolutions obtained by their superposition (bottom lines). (a) Periodic solution (purple) and the fold eigenmode (gray) superposed in two ways. (b) Singlefold solution (violet) and the periodic eigenmode (gray). (c) Singlefold solution (teal) and the splitting eigenmode (gray). (d) Twofold solution (green) and the translational attraction or repulsion eigenmode (gray). (e) Twofold solution (yellow) and the rolling attraction or repulsion eigenmode (gray).

identified. Such a study is beyond the scope of the present work.

V. CONCLUSIONS

In this article, we reported on the existence of multifold solutions in a thin floating elastic sheet of finite length with hinged boundary conditions. Starting from known large amplitude periodic solutions [5], we used numerical continuation to uncover a series of solution branches that bifurcate from the periodic (wrinkle) branch as a function of the load P or the associated compression Δ. Each branch consists of an array of localized (fold) solutions. Symmetric and antisymmetric singlefold solutions, which are well known for the infinite sheet case [32], are found to bifurcate from branches of distinct periodic states and inherit their symmetry properties. The multifold states with $m = 2, 3, \ldots$ folds in the domain bifurcate from the periodic states in subsequent bifurcations and are, we believe, reported here in detail for the first time.

Based on our numerical continuation results, we performed a weakly nonlinear analysis of the multifold solutions. These states form as a result of a slow spatial modulation of the periodic wrinkle solutions. The spatial modulation satisfies an amplitude equation whose solutions can be written down in terms of Jacobi elliptic functions. The results determine the branches of multifold solutions in parameter space and match the numerical continuation results remarkably well. In particular, we determined the energy of multifold states and showed that the energies of like-number multifold states are almost equal, with energy gaps that become exponentially small as the sheet length increases [see Eq. (24)].

Finally, we also studied the stability of both the periodic and multifold solutions within a variational framework. We showed numerically that the symmetric and antisymmetric singlefold solutions are both stable, but that only one of them bifurcates from a stable periodic branch and so inherits its stability. We also showed that all the twofold solutions are unstable, but with a common instability mode characterized by the mutual attraction or repulsion of folds (see Sec. IV B 3). However, the relevant eigenvalue comes very close to zero as the localization increases, implying that the transition to a singlefold state requires essentially exponentially long times. This result is in agreement with the numerical simulations in Ref. [22] (with clamped boundary conditions) in which a threefold state was observed to decay into a singlefold state but did so so slowly that it was thought to be stable. We expect that future numerical simulations of floating elastica will provide further insight into the decay and annihilation of folds. These transient dynamics will depend sensitively on assumptions about the dissipative processes acting in the system. For example, in Ref. [22] the substrate is taken to obey 2D-Stokes flow laws. Although this type of dynamical behavior is beyond the scope of the variational framework we present, we stress that in the final equilibrium state there is no flow in the liquid substrate and hence that this state should be independent of the details of the dissipative processes that take the system to this state. However, with the addition of dissipative terms the theory would no longer be an energy minimization problem and the details of the stability calculations performed in Sec. IV B would inevitably change.

These results have been obtained for the special case of hinged boundary conditions. However, some numerical experiments employ clamped boundary conditions, see, e.g., Ref. [4], and in this case the route to localization appears to be different. Thus, an extension of the type of analysis performed here to the case of clamped boundary conditions $\phi = \phi'' = 0$ at $s = \pm L/2$ would also be valuable.

Our results can be used to provide a rule of thumb for experiments employing hinged boundary conditions where localization of wrinkles into folds is crucial. Multifold solutions may emerge naturally in certain geometries (for instance, in a floating elastic annulus, or an indented circular sheet or a centrifugally driven elastica [33–35]). The prediction of the energy gap between multifold and singlefold states obtained here can be used to determine which states can emerge deterministically or stochastically in the presence of thermal noise. This is of particular importance in microscopic-scale experiments [36,37] and in experiments in which the floating raft is granular [38]. Although in most experiments

folds are allowed to form spontaneously, our calculations also provide a basis for predicting the outcome of experiments with manually induced folds, which may be of particular interest in technological applications.

ACKNOWLEDGMENTS

This work was partially funded by the Berkeley-Chile Fund for collaborative research and Conicyt-USA Grant No. PII20150011. L.G. acknowledges support by Conicyt/Becas Chile de Postdoctorado Grant No. 74150032, Conicyt PAI/IAC Grant No. 79160140 and Fondecyt/Iniciación Grant No. 11170700. We are grateful to Enrique Cerda, M. Clerc, J. Marín, and P. Gandhi for fruitful discussions and a referee for suggestions that helped improve the paper.

APPENDIX A: JACOBI ELLIPTIC INTEGRALS

The quantities related to A in Sec. III B 2 can be written in terms of fundamental Jacobi elliptic integrals,

$$\left(\overline{A^{\,2}_{\rm dn}}, \overline{A^{\,2}_{\rm cn}}\right) = 2^4\kappa^2(D_2, C_2),$$
$$\left(\overline{A'^2_{\rm dn}}, \overline{A'^2_{\rm cn}}\right) = 2^4\kappa^4(D_2', C_2'),$$
$$\left(\overline{A^{\,4}_{\rm dn}}, \overline{A^{\,4}_{\rm cn}}\right) = 2^8\kappa^4(D_4, C_4),$$

where the coefficients $D_2, C_2, D_2', C_2', D_4, C_4$ are given, respectively, by the following mean values of the Jacobi elliptic functions:

$$D_2 \equiv \overline{\mathrm{dn}_k^2} = 1 - I(k),$$
$$D_2' \equiv \overline{\mathrm{dn}_k'^2} = \tfrac{1}{3}[k^2 - (2-k^2)I(k)],$$
$$D_4 \equiv \overline{\mathrm{dn}_k^4} = \tfrac{1}{3}[(3-k^2) - 2(2-k^2)I(k)],$$
$$C_2 \equiv \overline{k^2\,\mathrm{cn}_k^2} = k^2 - I(k),$$
$$C_2' \equiv \overline{k^2\,\mathrm{cn}_k'^2} = \tfrac{1}{3}[k^2 - (2k^2-1)I(k)],$$
$$C_4 \equiv \overline{k^4\,\mathrm{cn}_k^4} = \tfrac{1}{3}[k^2(3k^2-1) - 2(2k^2-1)I(k)].$$

APPENDIX B: EXPANSION OF FUNCTIONALS

Consider a small perturbation of a solution y_0 satisfying the variational problem, $y = y_0 + \delta y$, where δy is assumed to be of order ε, i.e., $\delta y = \varepsilon y_1 \neq 0$ and $y_1 \sim \mathcal{O}(1)$:

$$y = y_0 + \varepsilon y_1.$$

The function $\phi(s)$ can be expanded in terms of ε,

$$\phi = \phi_0 + \varepsilon\phi_1 + \varepsilon^2\phi_2 + \dots$$

and likewise for the load P,

$$P = P_0 + \varepsilon P_1 + \dots$$

and the compression and energy functionals,

$$\Delta = \Delta_0 + \varepsilon\Delta_1 + \varepsilon^2\Delta_2 + \dots,$$
$$E = E_0 + \varepsilon E_1 + \varepsilon^2 E_2 + \dots,$$
$$G = G_0 + \varepsilon G_1 + \varepsilon^2 G_2 + \dots.$$

Each term in these expansions can be obtained from the definitions of these relevant quantities (Sec. II A). For instance, the function ϕ is related to y through $\dot{y} = \sin\phi$, and it can be shown that the first- and second-order terms in the expansion of ϕ are, respectively,

$$\phi_1 = \sec\phi_0\,\partial_s y_1,$$
$$\phi_2 = \tfrac{1}{2}\tan\phi_0\sec^2\phi_0(\partial_s y_1)^2.$$

Analogously, the functionals Δ and E can be written as

$$\Delta = \Delta_0 + \varepsilon\left(\frac{\delta\Delta}{\delta y}, y_1\right) + \varepsilon^2\left(y_1, \frac{\delta^2\Delta}{\delta y^2}y_1\right),$$
$$E = E_0 + \varepsilon\left(\frac{\delta E}{\delta y}, y_1\right) + \varepsilon^2\left(y_1, \frac{\delta^2 E}{\delta y^2}y_1\right),$$

where Δ_0 and E_0 and their functional derivatives are evaluated at the solution y_0. For the sake of simplicity, we only consider here the terms that are relevant for the stability analysis. For the displacement, we obtain

$$\frac{\delta\Delta}{\delta y} = \tan\phi_0 D_s, \tag{B1}$$
$$\frac{\delta^2\Delta}{\delta y^2} = D_s^\dagger\Sigma_s^\Delta D_s, \tag{B2}$$

while for the energy,

$$\frac{\delta^2 E}{\delta y^2} = D_{ss}^\dagger\Sigma_{ss}^E D_{ss} - D_s^\dagger\Sigma_s^E D_s + \Sigma_0^E, \tag{B3}$$

where D_s and D_{ss} are, respectively, first- and second-order linear differential operators and $D_s^\dagger$ and $D_{ss}^\dagger$ are the corresponding adjoint operators. The scalar quantities Σ_s^Δ, Σ_0^E, Σ_s^E, Σ_{ss}^E are given by

$$\Sigma_s^\Delta \equiv \frac{1}{2}\sec^3\phi_0,$$
$$\Sigma_0^E \equiv \frac{1}{2}\sec^2\phi_0(y_0\dot{\phi}_0 + \cos\phi_0),$$
$$\Sigma_s^E \equiv \frac{1}{4}y_0^2\sec^3\phi_0 + \left[\dot{\phi_0}^2\left(\frac{1}{2} + \tan^2\phi_0\right) + \ddot{\phi}_0\tan\phi_0\right]\sec^2\phi_0,$$
$$\Sigma_{ss}^E \equiv \frac{1}{2}\sec^3\phi_0.$$

A straightforward calculation shows that the free-energy second-order term G_2 is given by

$$G_2 = \left(y_1, \frac{\delta^2 G}{\delta y^2}y_1\right) - P_1\left(\frac{\delta\Delta}{\delta y}, y_1\right),$$

where the second-order functional derivative is simply

$$\frac{\delta^2 G}{\delta y^2} = \frac{\delta^2 E}{\delta y^2} - P_0\frac{\delta^2\Delta}{\delta y^2}.$$

Notice that the functional derivatives have been introduced in symmetrical form, which simplifies the numerical calculations of Sec. IV B.

[1] L. Pocivavsek, R. Dellsy, A. Kern, S. Johnson, B. Lin, K. Y. C. Lee, and E. Cerda, Science **320**, 912 (2008).
[2] H. Diamant and T. A. Witten, Phys. Rev. Lett. **107**, 164302 (2011).
[3] B. Audoly, Phys. Rev. E **84**, 011605 (2011).
[4] M. Rivetti and S. Neukirch, J. Mech. Phys. Solids **69**, 143 (2014).
[5] O. Oshri, F. Brau, and H. Diamant, Phys. Rev. E **91**, 052408 (2015).
[6] G. W. Hunt, M. A. Peletier, A. R. Champneys, P. D. Woods, M. A. Wadee, C. J. Budd, and G. J. Lord, Nonlin. Dynam. **21**, 3 (2000).
[7] J. M. T. Thompson and A. R. Champneys, Proc. R. Soc. London A **452**, 117 (1996).
[8] A. R. Champneys and J. M. T. Thompson, Proc. R. Soc. London A **452**, 2467 (1996).
[9] A. R. Champneys and M. D. Groves, J. Fluid Mech. **342**, 199 (1997).
[10] J. Burke and E. Knobloch, Phys. Rev. E **73**, 056211 (2006).
[11] E. Knobloch, Annu. Rev. Condens. Matter Phys. **6**, 325 (2015).
[12] G. Iooss and M. Pérouème, J. Diff. Eq. **102**, 62 (1993).
[13] G. Kozyreff and S. J. Chapman, Phys. Rev. Lett. **97**, 044502 (2006).
[14] S. J. Chapman and G. Kozyreff, Physica D **238**, 319 (2009).
[15] J. P. Gaivão and V. Gelfreich, Nonlinearity **24**, 677 (2011).
[16] A. Bergeon, J. Burke, E. Knobloch, and I. Mercader, Phys. Rev. E **78**, 046201 (2008).
[17] J. Burke and E. Knobloch, in *Dynamical Systems, Differential Equations and Applications*, edited by X.-J. Hou, X. Lu, A. Miranville, J.-Z. Su, and J.-P. Zhu, Discrete Cont. Dynam. Syst. Suppl.-September (AIMS, 2009), pp. 109–117, doi:10.3934/proc.2009.2009.109.
[18] L. A. Peletier and W. C. Troy, *Spatial Patterns: Higher Order Models in Physics and Mechanics* (Birkhäuser, Basel, 2006).
[19] J. Burke and E. Knobloch, Phys. Lett. A **360**, 681 (2007).
[20] J. Burke and E. Knobloch, Chaos **17**, 037102 (2007).
[21] M. Rivetti, Comptes Rendus Mécanique **341**, 333 (2013).
[22] G. R. Marple, P. K. Purohit, and S. Veerapaneni, Phys. Rev. E **92**, 012405 (2015).
[23] O. Oshri and H. Diamant, Soft Matter **12**, 664 (2016).
[24] O. Oshri and H. Diamant, Phys. Chem. Chem. Phys. **19**, 23817 (2017).
[25] F. Brau, P. Damman, H. Diamant, and T. A. Witten, Soft Matter **9**, 8177 (2013).
[26] E. Cerda and L. Mahadevan, Phys. Rev. Lett. **90**, 074302 (2003).
[27] E. Doedel, H. B. Keller, and J. P. Kernevez, Int. J. Bifurcat. Chaos **1**, 493 (1991).
[28] E. Doedel, H. B. Keller, and J. P. Kernevez, Int. J. Bifurcat. Chaos **1**, 745 (1991).
[29] E. J. Doedel, A. R. Champneys, F. Dercole, T. Fairgrieve, Y. Kuznetsov, B. Oldeman, R. Paffenroth, B. Sandstede, X. Wang, and C. Zhang, *AUTO-07P: Continuation and Bifurcation Software for Ordinary Differential Equations* (Department of Computer Science, Concordia University, Montreal, Canada, 2008).
[30] F. Brau, H. Vandeparre, A. Sabbah, C. Poulard, A. Boudaoud, and P. Damman, Nat. Phys. **7**, 56 (2010).
[31] A. C. Chiang and K. Wainwright, *Fundamental Methods of Mathematical Economics* (McGraw-Hill/Irwin, Boston, MA, 2013), 4th ed.
[32] H. Diamant and T. A. Witten, Phys. Rev. E **88**, 012401 (2013).
[33] J. D. Paulsen, E. Hohlfeld, H. King, J. Huang, Z. Qiu, T. P. Russell, N. Menon, D. Vella, and B. Davidovitch, Proc. Nat. Acad. Sci. USA **113**, 1144 (2016).
[34] J. D. Paulsen, V. Démery, K. B. Toga, Z. Qiu, T. P. Russell, B. Davidovitch, and N. Menon, Phys. Rev. Lett. **118**, 048004 (2017).
[35] G. D. Carvalho, H. Gadêlha, and J. A. Miranda, Phys. Rev. E **90**, 063009 (2014).
[36] A. Gopal, V. A. Belyi, H. Diamant, T. A. Witten, and K. Y. C. Lee, J. Phys. Chem. B **110**, 10220 (2006).
[37] B. D. Leahy, L. Pocivavsek, M. Meron, K. L. Lam, D. Salas, P. J. Viccaro, K. Y. C. Lee, and B. Lin, Phys. Rev. Lett. **105**, 058301 (2010).
[38] E. Jambon-Puillet, C. Josserand, and S. Protière, Phys. Rev. Materials **1**, 042601 (2017).